Continuum description of granular flows: Simulation and experiment

Eirik G. Flekkøy and Knut Jørgen Måløy
Department of Physics, University of Oslo, P.O. Box 1048 Blindern, 0316 Oslo 3, Norway
(Received 2 February 1998)

Granular flows with strong hydrodynamic effects are studied numerically and experimentally. We introduce a model for grain flow in the presence of an interstitial gas in the approximation that inertia may be neglected. The model thus describes the grains as moving at their local terminal velocity relative to the interstitial gas, which is described by a local Darcy law. In addition to these two fields there is also a fluidization field that turns the granular motion on or off. This allows for the description of stagnant zones inside a granular flow as well as a free surface and heap formation. Experiments are carried out to study both a simple bubble rising through a tube and the more complex flow of grains out through a hopper. There is a reasonable quantitative agreement between experiment and simulation for the bubble flow. In the hopper flow the stagnation zones forming on the sides of the hopper during outflow are compared. Simulations and experiments agree quantitatively to the level of exponents characterizing the stagnation zones. In contrast to earlier experiments the present experiments use smooth grains and geometrically rough walls. This causes the present exponent to differ from that obtained in the earlier experiments. We finally apply the model to study the dynamics of a two-dimensional bubble. [S1063-651X(98)14106-5]

PACS number(s): 83.50.−v, 83.70.Fn, 47.11.+j

I. INTRODUCTION

Recently much effort has been devoted to the modeling and description of granular flows [1–3]. Like all dynamic systems, granular flows obey the basic conservation laws of mass, momentum, and energy. These conservation laws can be cast in the form of differential equations. However, in order to make such a description useful, constitutive equations are needed, in particular relations between strain and stress [1], and an equation of state. Since the validity of such constitutive relations depends strongly on the granular material at hand as well as its dynamical state, general continuum descriptions of granular flows are difficult, if not impossible. While it is true that existing descriptions may work well for strongly excited granular media, they are not applicable when the medium is less excited.

In hydrodynamics a wide variety of phenomena are described by the Navier Stokes equations for incompressible fluid flow. Since no analogous unified descriptions for granular flows exists, it is important to examine carefully the regimes of validity of each separate model. In most cases of interest, this cannot be done without direct experimental verification.

While current efforts to understand experiments of granular dynamics have largely focused on molecular dynamics simulations [4], a wide variety of simplified descriptions have also been studied. There are several models for granular flows that are based on simple kinematic rules for the motion of individual grains [5–7]. Although these models may produce grain formations, like heaps of realistic shape, they lack a realistic dynamic description.

Among the models that focus on dynamic aspects of granular flows there exist various continuum descriptions [8–11] as well as cellular automata models that seek to capture some essential part of the physics [3]. For the case of fluidized beds [12] continuum descriptions that describe the state of granular material excited by the flow of gas as an in-viscid liquid, have been studied [13]. In general these models describe granular flows that resemble the flow of fluids.

However, many granular flows are not strongly excited. A salient feature of such ''cooler'' flows is the continuous transition between solidlike behavior, where the material is kept in place by the walls of its container, to fluidlike behavior where there are continuous internal deformations. This kind of behavior appears not to have been previously studied by continuum models—although it has frequently been observed in experimental studies, for instance, in Refs. [14,15].

The purpose of the present paper is to investigate a continuum model that describes both the transition between the solidlike and the fluidlike behavior, and the dynamics of the flow. We specialize to the case of dry granular flow, which is strongly influenced by interstitial gas. The description of this flow is similar to that of fluidized beds [16]. However, as in cellular automata treatments of granular flows, the spirit of the present modeling emphasizes simplicity more than accuracy. In this spirit we propose a simple dynamical picture based mainly on the equations of mass conservation. The central simplification of the fluidlike dynamics relative to earlier models is the neglect of inertial effects in both the granular and gas phase. The aim is to model large scale features rather than details of the flow.

In order to describe the solid-fluid transition of the granular material, henceforth called sand, we assume that above a certain threshold density ρ_0 it behaves as a solid block connected with the walls of the container, whereas it behaves as a fluid governed by local drag forces where the density is below the threshold value. This means that where the density becomes larger than the threshold, the sand velocity is set to zero corresponding to solidification. In a real system, where momentum conservation holds, this would imply that momentum was absorbed by the surrounding walls. In our model description this momentum transfer is not explicit; only its effect of keeping the grains in place is taken into

account. The communication between the solid and fluid phases takes place on the boundary between them.

The continuum equations to be derived are solved by the use of a lattice Boltzmann model [17]. This model resembles a finite difference method in the way it treats the fluid phase, and could be replaced by such a method there. However, the model has a particularly useful aspect in providing a simple physical scheme for the solid-fluid boundary interaction. The model is based on the exchange of mass along links between lattice sites, and while the solid sites are otherwise frozen they are allowed to exchange mass with the fluid sites along the links to them.

To examine and validate the model we study three types of flow, two of which depend strongly on the interstitial gas and one in which the internal transition between solidlike and fluidlike behavior is the dominant feature. The gas dominated flows both involve rising bubbles of air through densely packed grains. In the first case a bubble of air rises through a straight vertical tube. As the bubble rises it dissolves, and the free surface near the top of the tube is lowered. Experiments and simulations agree on the large scale features in a rough quantitative sense. In the second gas-dominated case we investigate the qualitative aspects of a rising two-dimensional bubble numerically. Both a characteristic bubble shape and a dynamic evolution of the free surface is obtained.

The case where gas interactions play a smaller role involves the granular outflow of a hopper with rough walls. In the experiments the grains are large, thus allowing the gas to pass easily through. The system is photographed with a charge-coupled device (CCD) camera at various times, and the resulting images are subtracted pixel by pixel to allow detection of stagnant zones. Even though inertia is thought to be important in the experiment and not included in the simulations, the experiments and simulations agree on the qualitative shape of the stagnant zones as well as the exponent that governs the relation between the hopper angle and the distance from the hopper opening to the stagnant zone. We find that this exponent differs significantly from earlier measurements by Baxter *et al.* [15] where smooth walls were used.

It is noted that the numerical method employed, while adequate for the simulations discussed, appears to lack the resolution necessary to deal realistically with system where small scale pressure differences are crucial for the dynamics. Such systems presently include the intermittent flow of sand in an hourglass [14].

II. THE MODEL

As a starting point of the description we define the local densities of sand and air. The sand mass density ρ_s is defined as the density per unit volume. This volume is occupied by both sand and air. We define the dimensionless density $\hat{\rho}_s = \rho_s/\rho_g$ where ρ_g is the density of the material that makes up the grains, in this case glass. Likewise we define the dimensionless density of air ρ as the mass of air per unit volume normalized by the density of air at atmospheric pressure in a random loose packing. We shall use the result given by Scott [18] for the porosity of a random loose packing of spheres. The value he obtained by extrapolating data obtained by measurements on a finite size container to an infinite container size was 0.40. Hence, in a random loose packing at atmospheric gas pressure $\hat{\rho}_s = 0.60$ and $\rho = 1.0$.

We shall take the threshold density below which the sand is allowed to move as that of the random loose packing. When $\hat{\rho}_s$ exceeds ρ_0 the motion of the sand is frozen relative to the walls. We shall refer to this state of the sand as *solidified*, and we shall call the state where $\hat{\rho}_s \leqslant \rho_0$ and the sand can move as *fluidized*.

The conservation of sand and air is described by the continuity equations

$$\partial_t \rho + \nabla \cdot \mathbf{j}_a = 0, \tag{1}$$

$$\partial_t \hat{\rho}_s + \nabla \cdot \hat{\mathbf{j}}_s = 0, \tag{2}$$

where the (normalized) mass currents of air and sand, $\mathbf{j}_a$, $\mathbf{j}_s = \rho_g \hat{\mathbf{j}}_s$, have been introduced. These currents are partly determined by the local Darcy law

$$\mathbf{j}_a = \rho\left(\mathbf{u}_s - \frac{\kappa}{\mu}\nabla P\right), \tag{3}$$

where the sand flow velocity $\mathbf{u}_s = \hat{\mathbf{j}}_s/\hat{\rho}_s$ and $\kappa = \kappa(\hat{\rho}_s)$ is the local permeability of the sand matrix, μ the dynamic viscosity of air, and P the interstitial air pressure. Equation (3) says that in the local rest frame of reference for the sand the air flow is proportional to the pressure gradient. We shall take the local permeability as that given by the Carman-Kozeny expression [19] for packings of spheres. It reads

$$\kappa(\hat{\rho}_s) = \frac{a^2}{9K}\frac{(1-\hat{\rho}_s)^3}{\hat{\rho}_s^2}, \tag{4}$$

where a is the sphere's radius and the constant $K \simeq 5$ is obtained experimentally for a random packing of spheres. The above Darcy law plays the role of a constitutive equation for the mass currents and relies on the flow to be governed by viscous—rather than inertial—forces, i.e., the pertinent Reynolds number must be small. In the experiments particles of diameter 50 and 65 μm are used. At terminal velocity for single particles in air the Reynolds number is less than 0.8, which in the present context will be considered marginally small. In the modeling of fluidized beds Eq. (3) is employed with an extra term that is second order in velocity [16]. This term can be neglected at small Reynolds numbers. For fluidized beds momentum equations both for the fluid and granular phases are used. The neglect of inertial terms constitute the main simplification in the present model. It should be noted, however, that while inertial forces may be negligible for single particles they may be important for the motion of clusters of particles.

In Appendix B we argue that the interstitial air will be isothermal when particles are sufficiently small. In that case the pressure is easily written in terms of the densities ρ and $\hat{\rho}_s$. It follows from the isothermal equation of state for an ideal gas that $\phi P \propto \rho$ where $\phi = 1 - \hat{\rho}_s$ is the porosity. By taking the gradient on both sides of this equation and then dividing by the equation itself we obtain

$$\frac{\nabla P}{P}=\frac{\nabla\rho}{\rho}+\frac{\nabla\hat{\rho}_s}{1-\hat{\rho}_s}. \tag{5}$$

Substituting this equation of state in Eq. (3) we get

$$\mathbf{j}_a=\rho\left[\mathbf{u}_s-\frac{\kappa P}{\mu}\left(\frac{\nabla\rho}{\rho}+\frac{\nabla\hat{\rho}_s}{1-\hat{\rho}_s}\right)\right] \tag{6}$$

as the governing equation for the flow of air.

Equations (1)–(6) do not fully determine the dynamic evolution of the conserved densities. The physical assumption we add to complete the description is that the sand flow immediately reaches steady state, i.e., we neglect the acceleration of the sand. This assumption is justified for the case of single small grains: The distance a spherical grain of glass of radius a needs to fall to reach terminal velocity is approximately $[a/(50\ \mu\mathrm{m})]^4\ 3$ cm if the particle is falling freely. In a dense packing where there is also an initial upwards flow of air this distance is likely to be significantly smaller. If grain accelerations thus are neglected the net force (per unit volume) acting on the sand must vanish, i.e., $\nabla P=\rho_s\mathbf{g}$, where $\mathbf{g}$ is the acceleration of gravity. We will substitute this relation in Eq. (3) to get an expression for $\mathbf{u}_s$. However, since we are neglecting inertial effects, we will have problems when the falling sand causes the air to move downwards, and, in the next time step, the sand again acquires terminal velocity in the moving air. This downwind instability may be avoided by simply imposing that the sand only feels air motion that reduces the sand velocity. The sand velocity is then prescribed by the following relation:

$$\mathbf{u}_s=\begin{cases}\mathbf{j}_a/\rho+(\kappa/\mu)\rho_s\mathbf{g} & \text{when} \quad |\mathbf{u}_s-\mathbf{j}_a/\rho|\leqslant\mathbf{u}_s\\ (\kappa/\mu)\rho_s\mathbf{g} & \text{when} \quad |\mathbf{u}_s-\mathbf{j}_a/\rho|>\mathbf{u}_s\\ \mathbf{0} & \text{when} \quad \rho_s\geqslant\rho_0.\end{cases} \tag{7}$$

Note that while the approximate Eq. (7) depends on the relative velocity $\mathbf{j}_a/\rho-\mathbf{u}_s$ only, the $\nabla\rho/\rho$ term in Eq. (6) depends on $\mathbf{j}_a/\rho$ through Eq. (1). Equations (7) and (6) are thus independent and fully determine the flow velocities $\mathbf{u}_a$ and $\mathbf{u}_s$. The physical reason for this is the approximation of vanishing accelerations in Eq. (7). By the above assumptions we have obtained a closed set of equations on the level of mass conservation, thus avoiding the complications of finding the correct constitutive equations that describe the flow of momentum or energy.

How do the density fields relax to a state as described by Eqs. (7) and (3)? This question is less obvious than in the case where a momentum equation is employed. When the first line of Eq. (7) is used to get the current value of $\mathbf{u}_s$ at time t_n, the previous value of $\mathbf{j}_a$ at time t_{n-1} is required. By combining the first line of Eqs. (7) and Eq. (3) to eliminate $\mathbf{j}_a$ we obtain the recursion relation

$$\mathbf{u}_s^{(n+1)}=\mathbf{u}_s^{(n)}+\left[\frac{\kappa^{(n)}}{\mu}(\rho_s^{(n)}\mathbf{g}-\nabla P^{(n)})\right]$$

$$=\sum_{k=0}^{n}\left[\frac{\kappa^{(k)}}{\mu}(\rho_s^{(k)}\mathbf{g}-\nabla P^{(k)})\right],$$

where the subscripts n and k denote the time at which the fields are evaluated and the last line follows by induction from the first. Upon convergence of $\mathbf{u}_s$ the densities must organize to give $\nabla P=\rho_s\mathbf{g}$. This happens when the downwind instability is handled as in Eq. (7).

Even though the description of the mass flows given by Eqs. (6) and (7) neglect all inertial effects, they will deal correctly with the time dependence caused by the variation of permeability and air pressure. Hence, when accelerations can be neglected the model will describe both the transient pressure relaxation and the overall evolution of the bubbles following from the semisteady velocities.

By rewriting Eqs. (7) and (6) in terms of dimensionless quantities, obtained by rescaling of the velocities by $U_0=\kappa(\rho_0)\rho_g g/\mu$, the densities by their stationary values, the distance by some characteristic length h, the pressure by P_0, and the time with h/U_0 it is seen that the physical system is characterized by the Péclet number $\mathrm{Pe}=U_0h/D_0$ where $D_0=\kappa(\rho_0)P_0/\mu$. When the above expressions for U_0 and D_0 are used, Pe takes the form

$$\mathrm{Pe}=\rho_g g h/P_0. \tag{8}$$

The Péclet number may be interpreted as a measure of the ratio of the convective flow rate of sand to the diffusive flow of air in the solid phase. It is also the ratio of pressure forces to gravity forces. For instance, a bubble of air rising in a tube full of sand is described by the Péclet number $\mathrm{Pe}=0.125$, when P_0 is taken as the atmospheric pressure, $h=0.5$ m and the density of glass $\rho_g=2.5\times10^3$ kg/m^3. Note that Pe depends on the background pressure P_0 but not on the permeability (particle radius) or viscosity. This is because the sand flow rate in still air and the air diffusivity depend on κ/μ in a way such that κ/μ cancels in Pe.

Among the other simplifications made in the model, the use of the approximate Carman Kozeny equation (4) for the permeability is important. It can be shown to hold reasonably well for packings that are sufficiently dense. Zick and Homsy [20] have demonstrated that there is agreement within 25% between the predictions of Eq. (4) and simulations of flow in periodic arrays of spheres when $\hat{\rho}_s>0.3$. For lower densities Eq. (4) becomes less accurate. Because of the stability criteria of the Boltzmann model [21], we have further introduced the cutoff condition on the permeability that $\kappa(\hat{\rho}_s<0.3)=\kappa(0.3)\equiv\kappa_{\max}$.

III. THE NUMERICS: A LATTICE BOLTZMANN MODEL

The lattice Boltzmann model that we introduce for the present purposes represents a generalization of a model for advection diffusion phenomena [21]. These phenomena are described by the advection diffusion equation

$$\partial_t\rho+\nabla\cdot(\rho\mathbf{u}-D\nabla\rho)=0, \tag{9}$$

where $\mathbf{u}=\mathbf{u}(\mathbf{x},t)$ is an arbitrary vector field and $D=D(\mathbf{x},t)$ a diffusivity, which may also depend on space and time. The equation describes the conservation of the density ρ, which is transported by the combined action of advection and diffusion. We will exploit the fact that Eqs. (1) and (2) can be

cast in the above form. In the following we briefly review how the lattice Boltzmann model works.

In general a lattice Boltzmann (LB) model [22] describes a fluid by a large number of particle populations [23] that move from site to site on a regular lattice, where they interact in collisions according to certain conservation laws. In the present case the lattice will be triangular. The lattice unit vectors connecting neighboring sites are $\mathbf{c}_i$, $i=1,\ldots,6$. While a finite difference approach would give a numerical solution to the conservation equations, a LB model is based directly on a conservative process, which in turn is described by the conservation equations. This is useful in implementing the boundary conditions.

The particle populations are denoted by $N_i(\boldsymbol{x},t)$. A common interpretation is to think of $N_i(\boldsymbol{x},t)$ as the probability of finding a particle at $\boldsymbol{x}$ at time t moving with unit velocity in one of the six lattice directions $i=1,\ldots,6$. However, we may also think of the N_i's as actual masses. The density ρ is defined as

$$\rho=\sum_{i=1}^{6} N_i \tag{10}$$

and the algorithm consists of a two-step procedure: First the particle probabilities are propagated to their neighboring sites according to their associated velocities, i.e., $N_i(\mathbf{x}+\mathbf{c}_i)$ is given the value of $N_i(\mathbf{x},t)$ for every $\mathbf{x}$. Second, the 6 N_i's undergo a local interaction that conserves the value of ρ. These two steps constitute the basic simulation time step and are described by the equation

$$N_i(\mathbf{x}+\mathbf{c}_i,t+1)=N_i(\mathbf{x},t)+\lambda[N_i(\mathbf{x},t)-N_i^{\mathrm{eq}}], \tag{11}$$

where λ is a free relaxation parameter of the model and the equilibrium distribution N_i^{eq} depends only on $\mathbf{u}(\mathbf{x},t)$ and $\rho(\mathbf{x},t)$ and is given as

$$N_i^{\mathrm{eq}}=\frac{\rho}{6}(1+2\mathbf{c}_i\cdot\mathbf{u}). \tag{12}$$

Note that since $\Sigma_i N_i^{\mathrm{eq}}=\rho$ and the propagation step conserves the values of the N_i's, Eq. (11) conserves ρ at every time step. At boundary sites the probabilities are propagated back into the directions from which they came. This gives a vanishing mass flux on the boundaries. By using a Chapman-Enskog expansion procedure [21] it is possible to show that the evolution of ρ resulting from Eq. (11) is indeed given by Eq. (9) in the limit of small spatial gradients in ρ. The diffusivity is given as

$$D=-\frac{1}{2}\left(\frac{1}{\lambda}+\frac{1}{2}\right). \tag{13}$$

Now, in order to solve Eqs. (1) and (2) we introduce two particle probabilities A_i and S_i that define the densities according to $\rho=\Sigma_i A_i$ and $\hat{\rho}_s=\Sigma_i S_i$. The corresponding equilibrium distributions are taken as

$$S_i^{\mathrm{eq}}=\frac{\hat{\rho}_s}{6}(1+2\mathbf{c}_i\cdot\mathbf{u}_s), \tag{14}$$

$$A_i^{\mathrm{eq}}=\frac{\rho}{6}\left(1+2\mathbf{c}_i\cdot\left[\mathbf{u}_s-\frac{\kappa(\hat{\rho}_s)D_a\nabla\hat{\rho}_s}{(1-\hat{\rho}_s)}\right]\right). \tag{15}$$

For every time step the current $\mathbf{j}_a$ is computed and the advection velocity $\mathbf{u}_s$ is given by Eq. (7). Also the discrete approximation of $\nabla\hat{\rho}_s$ must be computed at every time step. There are now two evolution equations that are equivalents of Eq. (11) for A_i and S_i and two corresponding relaxation parameters λ_A and λ_S. The first of these is chosen as $\lambda_A=-2/(4D_A+1)$ with $D_A=\kappa(\hat{\rho}_s)P_0/\mu$ where P_0 is taken to be the constant initial average pressure.

The parameter λ_S determines a diffusivity D_S for the transport of $\hat{\rho}_s$, i.e., an additional term $D_S\nabla\hat{\rho}_s$ on the right hand side of Eq. (7). For reasons of numerical stability this term cannot be set to zero. Hence, even though D_S is chosen as small as numerically possible, there will be a diffusive smoothening of sharp fronts in the sand density profiles.

Since Eq. (7) predicts a faster flow of dilute than dense regions, fronts of increasing gradients in $\hat{\rho}_s$ may form. In particular, if sand is settling down through stationary gas lower values of ρ_s propagate faster than higher values and sharp shocks may form. This is seen in sedimenting beds. On the other hand, it may be shown [16] that, due to the lack of inertia, small perturbations during settling in a homogeneous ρ_s are linearly stable. The finite diffusivity D_S will counteract the formation of shocks. Furthermore, for the dynamics to be given by Eqs. (6) and (7) it is necessary that the scale over which the densities vary is significantly larger than the scale of the lattice constant [21]. For this reason as well as that of numerical stability, D_s must be nonzero.

Theoretically it would have been more elegant not to have the $\nabla\rho_s$ dependence in A_i^{eq}. It is possible to obtain the same macroscopic equations (1) and (2) by instead having a term linear in $S_i-S_i^{\mathrm{eq}}$ in the evolution equation for A_i. However, this solution is numerically unstable.

In order to describe the solid fluid boundary a Boolean field $C(\mathbf{x},t)$ is introduced. At ''solidified'' sites where $\hat{\rho}_s \geqslant \rho_0$ $C(\mathbf{x},t)=1$, otherwise it is 0. The interaction between the fluid and solid phases that is responsible for the dynamic transition between the two takes place along the bonds that connect solid and fluid sites. The mass exchange along these bonds is free, just as in the fluid phase. This is illustrated in Fig. 1. In the solid region the dynamics of the sand densities is otherwise frozen in the sense that the particle populations are simply not touched. Equation (6), which governs the air dynamics, then reduces to the simple diffusion equation.

As the sand mass transport between the solid and fluid phases is proportional to the density difference between the adjacent solid and fluid sites, the solid-fluid interaction is diffusive in nature. The existence of the granular diffusivity D_s adds to this picture. It is instructive to work out a simple example of the steady surface boundary layer that the model contains: Take the case where the boundary of the solid region forms a straight line at an angle Θ to the horizontal and assume for simplicity that the air current $\mathbf{j}_a=0$. We may then obtain the surface current $J_{\parallel}=\int dz' j_{s\parallel}$ where z' is a coordinate normal to the boundary and $j_{s\parallel}$ is the parallel component of the full granular mass current $\mathbf{j}_s=-D_s\nabla\rho_s+\rho_s\mathbf{u}_s$. Since $\mathbf{j}_a=0$ Eq. (7) reduces to $\mathbf{u}_s=\kappa/\mu\rho_s\mathbf{g}$. At steady state $j_{s\perp}$

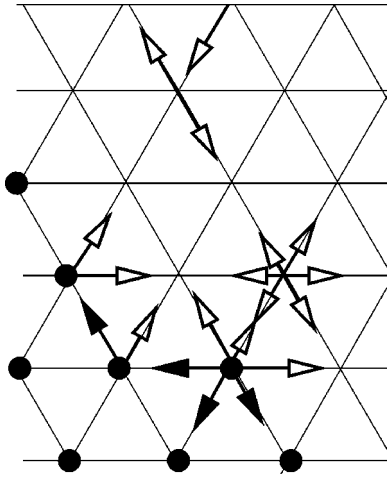

FIG. 1. Particle populations in the Boltzmann model. The sites marked with a ● are solidified sites. Filled arrows represent stationary particle populations while empty arrows represent moving particles. All directions on every site has an associated particle population. Only selected ones are shown.

$=0$ and $D_s(\nabla\rho_s)_\perp=(\kappa\rho_s^2/\mu)g\cos\Theta$. Hence $j_{s\parallel}=\rho_s u_{s\parallel}=(\kappa\rho_s^2/\mu)g\sin\Theta=\rho_s u_{s\perp}\tan\Theta=D_s(\nabla\rho_s)_\perp\tan\Theta$. Integration of the right-hand side gives

$$J_\parallel=\rho_0 D_s\tan\Theta, \tag{16}$$

where, as before, ρ_0 is the density in the solid phase. The physical picture behind this equation is that of a randomly excited thermal gas in a gravity field, where particles that tear loose from the solid phase receive a certain average constant velocity. In Appendix A the density profile across a $\Theta=0$ interface is studied in some more detail, and it is shown that it confirms well to analytic predictions.

The surface flow in the model implies that heaps of granular material will slowly decay to a flat state, as if they were being gently shaken. However, as will be seen in Sec. IV C it is possible to identify an interface shape on the time scale of the simulation as the final decay of the interface happens more slowly than the main flow itself.

The discontinuous transition between the solidified and fluidized phase is based on the physical approximation that all grain-grain contacts are instantly replaced by hydrodynamic grain interactions when the density falls below the threshold density.

It is a well established fact that a granular medium must dilate (expand) in order to move relative to itself or its surroundings [24,25]. The dilatency necessary for motion relative to a smooth wall might be significantly smaller than the dilatency needed for internal shear. In the present model, however, we make no such distinction between small and large dilatencies. In the simulations discussed in Sec. IV A the dilatency needed for the motion relative to the walls to begin is determined by the initial excess density.

IV. EXPERIMENTS AND SIMULATIONS

In order to see what can be learned from the present model we now turn to the direct comparison of it by two selected experiments.

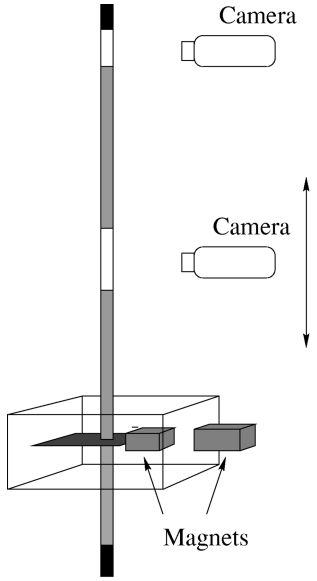

FIG. 2. The experimental bubble setup. A plate with a hole is pulled to the right by an external magnet, thus allowing the bubble to form within the sealed system. The bubble motion and the top interface are recorded by two video cameras.

A. Bubble in a tube

One of the simplest possible applications of the model to a case where gas interactions are strongly governing the flow is a simple one-dimensional flow through a tube. In the experiments, the flow is, of course, three dimensional.

Bubble dynamics have been studied extensively in the case of fluidized beds, and an approximate analytic solution of corresponding continuum equations for mass and momentum conservation has been obtained by Davis and Taylor [26]. While this solution neglects boundary effects and depends on the inertia of a fluidized medium, the present numerical study focuses on a drag dominated bubble in an initially close packing in the presence of walls. The experimental setup here is similar to that used in the work of Raafat *et al.* [27] who also introduce an analytic description of the nonlinear essentially one-dimensional motion of granular plugs. However, while their work deals with the dynamics of a finite ''bubble'' of sand moving through air, the present setup deals with the complementary state where a bubble of air creates a local motion in a bed of stationary sand. The present description and the corresponding simulations are two dimensional and can easily be extended to three dimensions.

In the experiment, illustrated in Fig. 2 the bubble was released at the bottom of a long vertical glass tube. The tube, which is closed on both sides, has an internal diameter of 5 mm, and a total internal length of 105.1 cm. The tube has two parts of length 5 cm and 100.1 cm, respectively. The upper part of length 100.1 cm was filled with small glass beads and the lower part 5 cm was filled with air at atmospheric pressure. Two types of glass beads of diameter $d=51\pm8$ μm and $d=65\pm9$ μm were used. A density of $\rho_s=1.38$ g/cm^3 was obtained by simply pouring the beads into the tube. To perform an experiment with an increased density, the $d=65$ μm particle packing was further compactified by tapping uniformly on the side walls. This gave a

density $\rho_s = 1.44$ g/cm^3. A shutter mechanism is placed between the upper and the lower tube. The shutter consists of a 0.5 mm thick aluminum plate with a hole of diameter 5 mm. Two small permanent magnets are mounted on each side of the plate, and an external permanent magnet was used to move the plate. The bubble propagation starts when the hole in the aluminum plate is in position with the tube. To prevent air leakage and to make the system transparent, the shutter mechanism is sealed in a piece of Plexiglas. Both the upper and the lower parts were initially kept at atmospheric pressure. To visualize the motion of the bubble and the top level of the sand we used two video cameras. The camera that recorded the bubble motion was mounted on a vertical translation stage to follow the bubble. The second camera recorded the motion of the top interface of the sand.

The bubble has a rather sharply defined top and bottom. The position of the upper and lower interface of the bubble as functions of time were easily determined from video recordings of the bubble motion. Also the position of the free surface on the top was easily defined.

In these experiments one should really consider two values of the dilation needed for the granular packing to start its motion. To move relative to the walls the static wall-particle friction must be relaxed. Due to the slight elasticity of the particles this requires a small dilation of the packing. This dilation will be larger if the walls are rough. To move relative to each other particles must be able to pass by each other. This internal shear motion requires a much larger dilatency, which may be of the order 10%. In the case of the flow in a smooth tube like the present one, an initial compactification of the packing may survive throughout the experiment [25]. This confirms that in order to move relative to the walls the packing need only reduce its density by a small fraction of the initial density.

In the simulations no wall friction exists, and the wall interactions are either on or off according to the value of $\hat{\rho}_s$. The bubble was initialized as a depletion of Gaussian shape in an otherwise constant density profile $\hat{\rho}_s = (1+q)\rho_0$. Initially the solidification field is therefore on outside the depletion. The term q is the relative excess compactification. Initially in the simulation a fluidization front propagates through the system, as illustrated in Fig. 3, thus reducing the density below ρ_0. For moderate values of q and significant values of the terminal velocity, which the particles are assumed to reach instantly, the layer of sites that become fluidized will have a sufficient mass transport away from the front to allow the next layer above to fluidize in the next time step. In this case the speed of the front will be between $\sqrt{3}/2$ and 1 lattice unit per time step, depending on the orientation of the lattice.

This rapid fluidization front, although realistic in appearance, only captures part of the physics in the experiment. In the experiments the packing must also loosen from the walls by the action of a rapidly propagating front. But here inertia, wall friction, and long range force network will all be potentially active mechanisms. Several questions regarding the fallout process from a region of grains supported by the walls are still open, both in this and related works [27].

In the simulations the delay of the free surface motion relative to the initialization of the bubble is sensitive to the value of q. On the other hand, the motion of the bubble itself, which takes place on a larger time scale than the front propagation, depends only weakly on q.

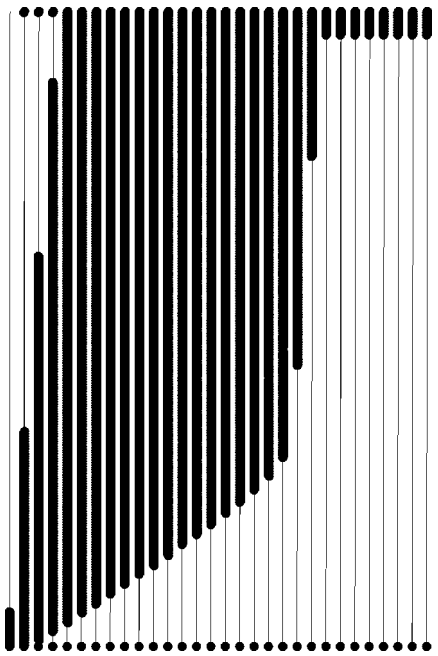

FIG. 3. Simulation: the fluidized region shown at a series of different times. Parameters are as in Fig. 4.

Figure 4 shows the time evolution of the sand density profiles in the simulations. The location of the bubble bottom and top as well as the position of the free surface was defined in these simulations as the position where the density was half way between its local minimum and maximum values. These positions are illustrated in a graphical way in Fig. 5, which also closely resembles the visual appearance of the experiment. The final comparison between experimental and simulation results is shown in Figs. 6 and 7. In the experiment the bubble location is determined by visual inspection. In the simulation, where the bubble undergoes some diffusive smearing, its extent is defined by the region where the density is below $(\rho_0 + \rho_{\min})/2$, where $\rho_{\min}$ is the minimum value of the density in the bubble. The position of the free surface is defined similarly, $\rho_{\min}$ is in this case the minimum value of the density above the surface. The time is normalized by the time T_0, which is the time the (extrapolated)

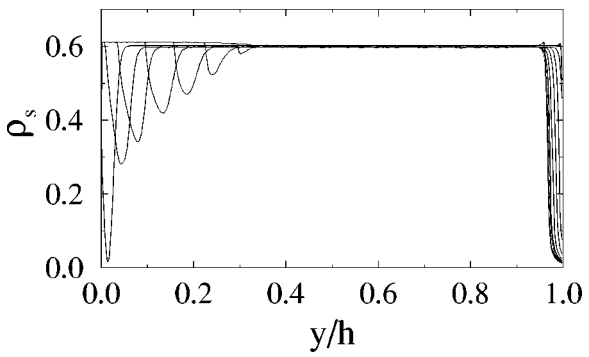

FIG. 4. Simulation: the dimensionless sand density profiles at different times. The system size is 512 by 1, $D_s = 0.001$ and the compactification parameter $q = 0.0025$.

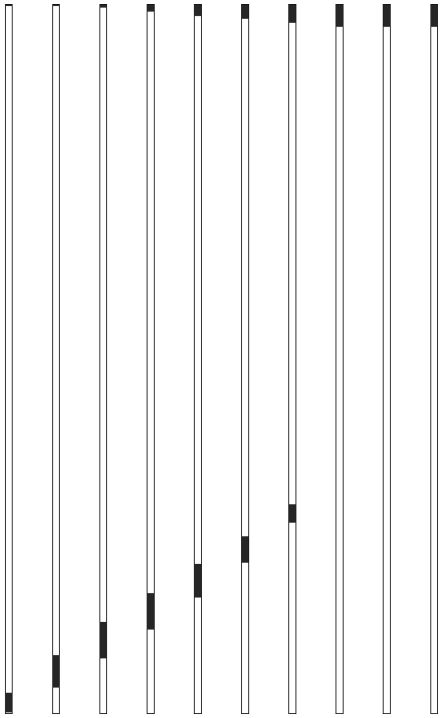

FIG. 5. The bubble and the top regions shown at a series of different times. The figure represents the same data as in Fig. 4.

bubble needs to reach the top of the sand packing. The positions are normalized with the position of the top surface h before the bubble was released. Both experiments and simulation agree that the velocity of the bubble is independent of its position and size. The agreement is fairly good both for the position where the bubble finally disappears, and for the top motion. In view of the simplifications introduced in the simulations this agreement is rather encouraging. However, it should be noted that both the interior shape of the bubble and its exact boundary positions are not captured by the simulations.

B. Stagnant regions and hopper flow

There are two main aspects of the modeling, the gas-grain interaction described by the comoving Darcy law and the grain-grain interactions introduced by the solid fluid transition rules. Here we investigate the latter in a simple hopper flow experiment. The solid-fluid–like transition is a uniquely granular phenomenon that is linked both to the static friction present between grains and the dilatency that is a prerequisite for granular motion.

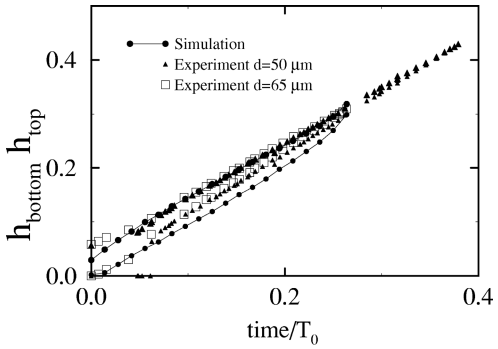

FIG. 6. The top and bottom positions of the bubble and the position of the top surface for the simulation and experiment. The positions are normalized by the tube length. Simulation parameters are as in Fig. 4. Here the lattice is 1×512 and $q=0.0025$.

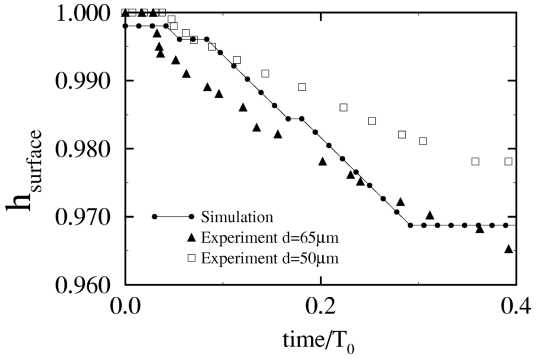

FIG. 7. The surface positions corresponding to the bubble positions shown in Fig. 6.

In the experiment a quasi-two-dimensional hopper consists of two glass plates separated a distance 5 mm apart. The inclined hopper side walls make an angle $\Theta/2$ with the vertical. These side walls are made rough by absorbing glass beads onto double-sided tapes, glued on the side-walls. The width of the orifice, initially closed with a piece of tape, is $D=10.1$ mm. The hopper was filled with glass beads of $d=1.0$ mm, and the flow was initiated by removing the tape at the orifice. To visualize the flow, pictures were taken with a high resolution (1500 times 1200 pixels) Kodak DCS 420 CCD camera. The stagnant zones become apparent by subtraction of the pictures with a picture before the flow started. As seen in Fig. 8 the stagnation zones will then appear as regions with much less noise than in regions with particle movement. Note that on account of the gluing of particles to the walls, a layer or two along the sides will always be stagnant. Figure 9 shows the corresponding simulations. These were carried out in an hourglass geometry in order to see the pile formation in the bottom as well. This pile has the same qualitative shape that is observed in experiments [7]. The distance d_c to the stagnant region from the orifice, as indicated in Fig. 8, was measured as a function of the hopper

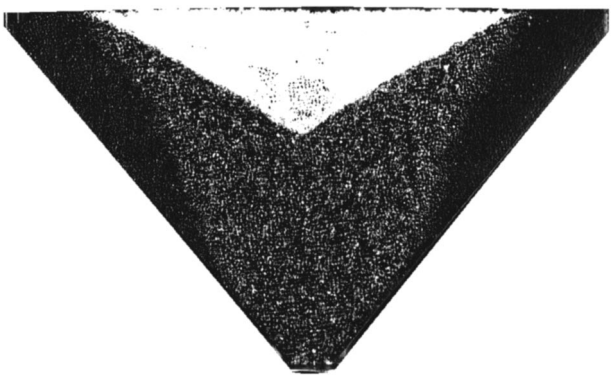

FIG. 8. Picture of the hopper flow experiment. This is a difference image obtained by subtracting an image before from an image during the flow. The stagnation zones, which are regions of no displacement, are made visible as distinct dark zones with very little noise.

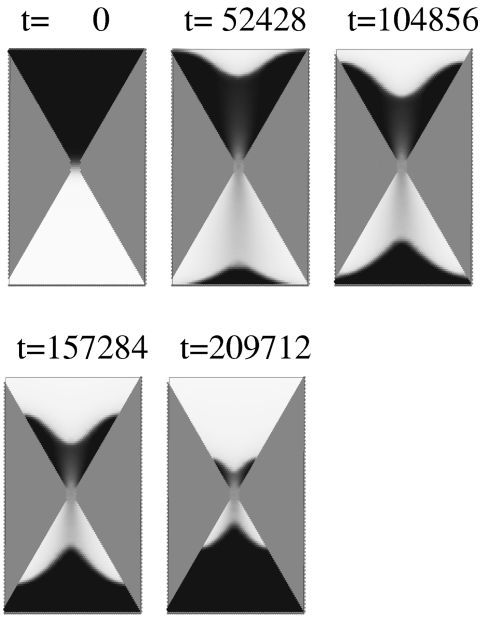

FIG. 9. Hopper flow. The granular density is shown on a linear gray scale where black corresponds to the highest density. The Péclet number Pe=0.12, $D_s=0.0005$, and the lattice is 64×128.

angle Θ. In the simulations the stagnant regions are directly available as the regions where the solidification field is on. Figure 10 shows this field as a function of time. In both experiment and simulations the lower position of the stagnant region was quite time independent, so that a single d_c could be defined. In the simulations the field $\hat{\rho}_s$ interacts with solidified sites in the same way as wall sites. Hence, the simulations model an experimental situation where the wall has the property of a collection of fixed grains. For that reason smooth walls were inadequate for comparison with the present simulations. This corresponds to walls with grains glued onto them as in the experiments. Figure 11 shows $1/d_c$ as a function of Θ for both the simulations and experiments. Both graphs are consistent with a linear dependence. This is in a striking contrast to the smooth wall experiments by Baxter and Behringer [15] who obtained an exponent of 2.2 ± 0.1. The prefactors are seen to differ in the experiment and the simulations though. These are expected to depend on grain-grain friction as well as the grain geometry and possibly size (see Fig. 12).

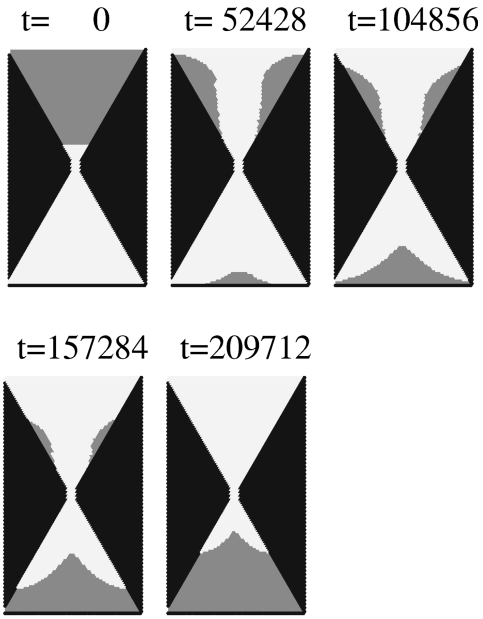

FIG. 10. The solidified region shown as dark gray corresponding to Fig. 9. The fluidized region is shown as light gray.

While the simulations do not include inertia, the experiment clearly does as the particles in the hopper opening are large and fall freely. The flow rate close to the stagnant zones, on the other hand, is very slow. However, it may still be affected by the inertia controlled central flow. Hence, it is not obvious *a priori* that the simulations are suited to capture the experimental behavior, and the results must be judged in view of that. It is therefore an encouraging observation that the stagnant zones indeed appear to be predictable by the present, inertialess model.

C. A two-dimensional bubble

Finally we present some purely numerical results for a two-dimensional bubble, which is shown in Fig. 12. The bubble was again initialized as a Gaussian depletion in an otherwise constant density field. The simulation parameters are given in the caption. In Fig. 13 the solidification field is shown as in Sec. IV B. The two main results of these simulations are the shape of the bubble, which shows a clear wedge shape in the bottom, and the evolution of the free surface. As is discussed in the Appendix, the free surface shape will change slowly in time, corresponding to the fact that there will be a small surface flow due boundary diffusion. However, in large simulations a separation of the time scale on which the main flow takes place and the time scale on which the surface flow takes place, is possible. Hence, the surface will have insufficient time to change between the end of the flow and the end of the simulations, and comparison between experiment and simulation will make sense.

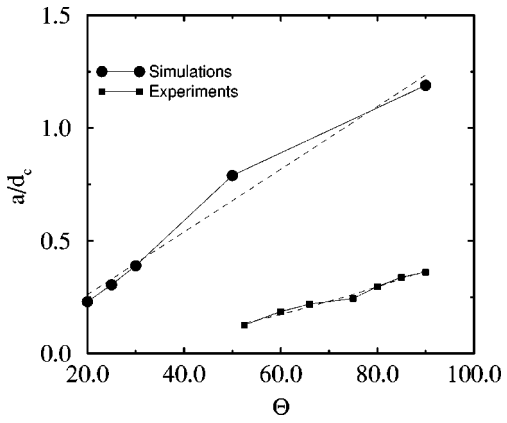

FIG. 11. The inverse distance $1/d_c$, where d_c is the distance between the hopper opening and the stagnation zone as a function of the hopper opening angle Θ. Both experiments and simulations are shown.

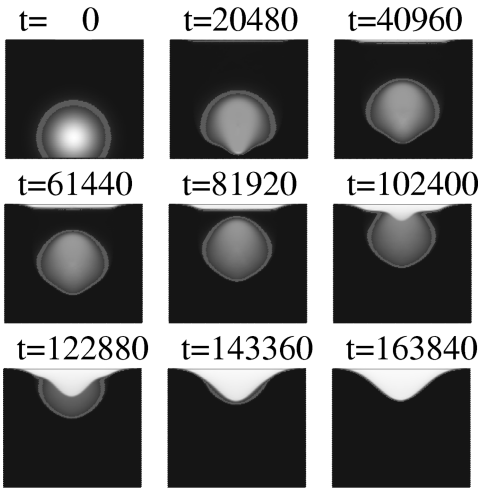

FIG. 12. A simulated two-dimensional bubble at different times. The Péclet is Pe=0.025, the granular diffusivity $D_s=0.0005$, and the lattice size 128×128. The gray outer rim of the bubble shows the region where the density is in the interval $0.3<\hat{\rho}_s<0.35$.

V. CONCLUSION

We have introduced a model for granular flow under the influence of an interstitial gas. We have tested the model by comparing its main features directly with experiments. This development has had three distinct parts:

(1) the development of the model as described by Eqs. (1) and (2) and the constitutive permeability;
(2) the development and implementation of the corresponding scheme for the numerical solution of this model by means of a lattice Boltzmann model;
(3) the experiment and interpretation necessary for the comparison with the theoretical results.

Although we have in part found quantitative agreement between experiment and simulations, we stress that part (2) of this development does not perfectly communicate between parts (1) and (3). This is due to the fact that the equations themselves pose serious numerical challenges, which are only partially solved by the present numerical scheme. This numerical scheme has successfully described the dynamics of a single bubble where details of local pressure variations are not crucial. Current numerical studies [28] aimed at modeling the intermittent flow in the ''ticking hourglass'' [14] indicate that this can be done with a model similar to the present one, but at the expense of solving explicit pressure and momentum equations.

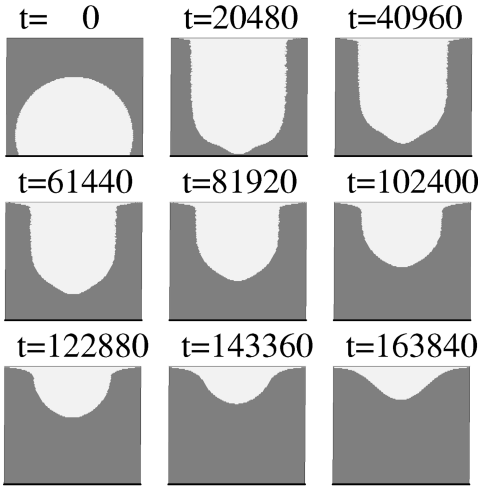

FIG. 13. The fluidized and solidified regions corresponding to Fig. 12. Again the solidified region is shown in dark gray and the fluidized region in white.

When grains fall through a gas at terminal velocity cooperative hydrodynamic effects, giving the local drag forces, will cause dilute regions of the particle cloud to fall faster than denser regions. This effect will cause shocks to form, and in experiments on granular pipe flow [27] sudden appearances of clogs are observed. Numerically this is an intrinsic mechanism of instability as it implies the divergence of density gradients. For this reason the numerical model used, which is a variant of a lattice Boltzmann model [17], cannot explore all the information that is in principle available through the governing equations at hand.

We were, however, able to predict quantitatively the motion of the bubble boundaries in a tube and the motion of the free surface. Moreover, the model was successful in the description of hopper flow with the boundary between flowing and stagnant regions. Further developments of numerical techniques to handle Eqs. (1) and (2) seem a promising route to improve insight on complexities of granular flows.

ACKNOWLEDGMENTS

The authors thank Thierry Le-Pennec and Hans Herrmann for valuable comments. The work was supported by the Norwegian Research Council (NFR) for Science and the Humanities under Grant No. 100339/431. The computations were done on the CM5 at Center National de Calcul Paralléle en Sciences de la Terre.

APPENDIX A: THE INTERFACE THICKNESS AND NUMERICAL STABILITY

The free surface of the sand will have a finite thickness as described by the Boltzmann model. The reason for this is the nonvanishing diffusivity in the sand current. In Eq. (7), which gives the sand mass current, we get an extra diffusive term $-D_s\nabla\rho_s$ on the right hand side. Hence, in the steady state when there is no mass flux, Eq. (7) takes the form

$$0=\frac{\kappa(\hat{\rho}_s)}{\mu}\rho_s^2\mathbf{g}-D_s\nabla\rho_s\,, \tag{A1}$$

where D_s is the small but nonzero diffusion constant. From Eq. (A1) it is possible to obtain an expression for the density profile across an interface oriented perpendicular to $\mathbf{g}$. If y is taken as a coordinate along $-\mathbf{g}$ we get

$$dy=-\frac{D_s\mu}{\rho_g g\hat{\rho}_s^2\kappa(\hat{\rho}_s)}d\hat{\rho}_s, \tag{A2}$$

which can also be written

$$\frac{\kappa_0 d\hat{\rho}_s}{\hat{\rho}_s^2\kappa(\hat{\rho}_s)}=-\mathrm{Pe}_s\frac{dy}{h} \tag{A3}$$

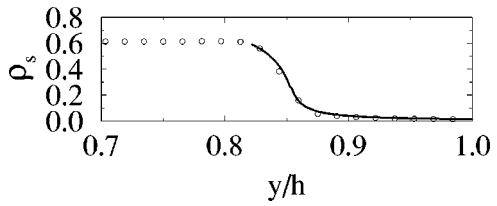

FIG. 14. The density $\hat{\rho}_s$ as a function of position across the free interface. The solid line shows theoretical values given by Eqs. (A4) and (A5) and ○ shows the simulations.

where we have introduced the Péclet number $\mathrm{Pe}_s = U_0 h/D_s$. Integrating this equation from a known density $\hat{\rho}_{s0}$ at y_0 and using Eq. (4) we immediately get

$$\hat{\rho}_s = 1 - \frac{1-\hat{\rho}_{s0}}{\sqrt{1 - 2\,\mathrm{Pe}_s[\hat{\rho}_{s0}^2/(1-\hat{\rho}_{s0})][(y-y_0)/h]}}. \quad \text{(A4)}$$

However, conforming to the stability criteria of the Boltzmann model [21], we have introduced the cutoff condition on the permeability that $\kappa(\hat{\rho}_s > 0.3) = \kappa(0.3) \equiv \kappa_{\max}$. Hence Eq. (A4) only describes the interface down to the cutoff density. For the $\hat{\rho}_s < 0.3$ region we must repeat the above exercise with $\kappa = \kappa_{\max}$. This gives the result

$$\hat{\rho}_s = \frac{\hat{\rho}'_{s0}}{1 + (\kappa_{\max}/\kappa_0)\mathrm{Pe}_s(y-y'_0)/h}, \quad \text{(A5)}$$

where $\hat{\rho}_s = \hat{\rho}'_{s0}$ at $y = y'_0$. Hence when $D_s \to 0$ and $\mathrm{Pe}_s \to \infty$ the density profile will be infinitely sharp.

When Pe_s is finite, the first part of the interface will have a characteristic thickness

$$\Delta y = \frac{h}{\mathrm{Pe}_s} = \frac{D_s}{U_0} = \frac{D_s h}{D_a \mathrm{Pe}}. \quad \text{(A6)}$$

The latter expression is relevant if, as in the simulations, Pe is fixed by the experimental value and D_s by numerical constraints [21]. In the simulations $D_s = 0.001(\text{lattice unit})^2/(\text{time step})$, $\mathrm{Pe}_s = 12$ and the characteristic width is 2 lattice units. The prediction of Eqs. (A4) and (A5) are plotted in Fig. 14 together with the results of a simulation. In view of the fact that the equations governing this result are obtained in the limit of vanishing density variations on the scale of the lattice constant, the magnitude of the width and the agreement with theory is remarkable.

There are at least three important criteria for the stability of the numerical model, one of which relate to the drift velocity and two of which relates to the magnitude of the density gradients. For stability and adherence to Eqs. (1) and (2) the drift velocity U_0 should be at least less than 0.1. In order to keep the gradients sufficiently small, the diffusion coefficients must be kept above certain minimum values. In practice this restriction is not so strict [21,29] and the minimum value can be chosen as $0.0005(\text{lattice unit})^2/(\text{time step})$ without too much error. Finally, the interface thickness cannot be too small. If the parameters of Eq. (A6) are chosen to give a too small interface thickness, numerical instability results. In Fig. 14 showing a one-dimensional simulation, agreement between theory and simulation is obtained for an interface thickness of 2–3 lattice sites. However, when the simulations are two dimensional, the minimum thickness is about 5–6 lattice units.

In an actual simulation this stability criteria limit the resolution of the results. The diffusive smearing of the sand density field can be estimated by the increase in the root mean square width Δz of a Gaussian profile. When the time is taken as $t = h/U_0$ where $U_0 = \mathrm{Pe}\, D_a/h$ the result is $\Delta z^2 = 2D_s t = 2D_s/(\mathrm{Pe}\, D_a)h^2$, i.e., the characteristic smearing distance

$$\frac{\Delta z}{h} = \frac{2D_s}{\mathrm{Pe}\, D_a}. \quad \text{(A7)}$$

According to Eq. (A6) the diffusivity D_s can be chosen smaller as $1/h$ when the system size is increased while keeping the interface width fixed. Hence, since a smaller D_s gives a smaller Δz, the resolution can be improved by increasing the system size. However, the relative spread only decreases as $1/\sqrt{h}$.

APPENDIX B: DISCUSSION OF THE ASSUMPTION OF AN ISOTHERMAL GAS

Air at atmospheric pressure is well described by the equation of state for an ideal gas. For sufficiently small particles the gas even follows the *isothermal* equation of state, which we shall employ. To justify this we must examine the time needed for heat to be absorbed by the grains and compare it to other relevant time scales. The shortest available such scale is the time t_c a particle spends in falling a distance a at terminal velocity. For this order-of-magnitude estimate we will approximate the description of the temperature evolution in the air with a simple diffusion equation. The thermal diffusivity is then given as $D_T = k/(\rho c_p)$, where k is the thermal conductivity [with units W/(K m)], c_p is the specific heat capacity at constant pressure [with units J/(K kg)], and ρ is the mass density. A local temperature variation will spread out diffusively according to the diffusion law $\Delta X^2 = 2D_T t$, where ΔX is the characteristic spatial extent of the local variation and t is time. In a not too loose packing of grains we can take $\Delta X = a$ and define the characteristic diffusion time $t_D = a^2/(2D_T)$. Comparing this time with the time t_c and inserting the proper physical constants for air we get a Péclet number $t_D/t_c \approx 1$ characterizing the thermal diffusion in stationary air. When the thermal conductivity is taken as that of glass we get $t_D/t_c \approx 30$. The first of these results shows that on the time scale t_c thermal diffusion alone is sufficient to smear out temperature variations in the air between particles. The second result shows that on the same time scale an external temperature difference will not be felt in the centers of the grains (still taken as equal size spheres). However, the heat capacity of the subvolume of the spheres that *will* feel the temperature difference in the time t_c greatly exceeds the heat capacity of the interstitial air even for particles of size up to 1 mm. Hence, temperature variations in the air will be absorbed by the spheres to a good approximation. For larger particles the Péclet number $t_D/t_c \propto a^3$ will increase. However, on time scales larger than t_c the velocity gradients in the air caused by the relative motion of the air

and grains will greatly enhance the temperature equilibration. In fact, the process is very similar to the process of hydrodynamic dispersion in porous media or fluidized beds where a *conserved* passive tracer is transported under the combined action of advection and diffusion inside a medium [30]. Such processes, which are used in industry to speed up mixing, are known to bring about fairly complete mixing already after the passing of a few distances a [31].

[1] J. T. Jenkins and S. B. Savage, J. Fluid Mech. **130**, 187 (1983).
[2] I. Goldhirsch and G. Zanetti, Phys. Rev. Lett. **70**, 1619 (1993).
[3] G. Peng and H. J. Herrmann, Phys. Rev. E **49**, 1796 (1994).
[4] J. Gallas, H. J. Herrmann, and S. Sokolowski, Physica A **189**, 437 (1992).
[5] H. Caram and D. C. Hong, Phys. Rev. Lett. **67**, 828 (1991).
[6] G. W. Baxter and R. P. Behringer, Physica D **51**, 465 (1991).
[7] J. J. Alonso and H. J. Herrmann, Phys. Rev. Lett. **76**, 4911 (1996).
[8] H. Hayakawa, S. Yue, and D. C. Hong, Phys. Rev. Lett. **75**, 2328 (1995).
[9] M.-L. Tan, Y. H. Qian, I. Goldhirsch, and S. A. Orzaag, J. Stat. Phys. **81**, 87 (1995).
[10] E. Manger, T. Solberg, and B. H. Hjertager, Int. J. Multiphase Flow **21**, 561 (1995).
[11] W. A. Beverloo, H. A. Leniger, and J. van de Velde, Chem. Eng. Sci. **15**, 260 (1961).
[12] D. Gidaspau, *Multiphase Flow and Fluidization* (Academic Press, San Diego, CA, 1994).
[13] J. F. Davidson, in *Mobile Particulate Systems*, edited by E. Guazzelli and L. Oger (Kluwer Academic Publisher, New York, 1995), p. 197.
[14] X. L. Wu *et al.*, Phys. Rev. Lett. **71**, 1363 (1993).
[15] G. W. Baxter and R. P. Behringer, Phys. Rev. Lett. **62**, 2825 (1989).
[16] G. M. Homsy, in *Disorder and Mixing* (Kluwer Academic Publisher, Dordrecht, 1988), pp. 185–201.
[17] E. Flekkøy, Ph.D. thesis, University of Oslo, 1993.
[18] G. D. Scott, Nature (London) **188**, 908 (1960).
[19] P. Carman, Trans. Inst. Chem. Eng. **15**, 150 (1937).
[20] A. Zick and G. Homsy, J. Fluid Mech. **115**, 13 (1982).
[21] E. G. Flekkøy, Phys. Rev. E **47**, 4247 (1993).
[22] G. McNamara and G. Zanetti, Phys. Rev. Lett. **61**, 2332 (1988).
[23] U. Frisch *et al.*, Complex Syst. **1**, 648 (1987).
[24] O. Reynolds, Philos. Mag. **20**, 469 (1885).
[25] T. L. Pennec *et al.*, report.
[26] R. M. Davies and G. I. Taylor, Proc. R. Soc. London, Ser. A **200**, 375 (1950).
[27] T. Raafat, H. J. Herrmann, and J. P. Hulin, Phys. Rev. E **53**, 4345 (1996).
[28] E. G. Flekkøy and K. J. Måløy (unpublished).
[29] E. G. Flekkøy, U. Oxaal, J. Feder, and T. Jøssang, Phys. Rev. E **52**, 4952 (1995).
[30] *Disorder and Mixing*, edited by E. Guyon, J.-P. Nadal, and Y. Pomeau (Kluwer Academic, Dordrecht, 1988).
[31] P. Rigord, A. Calvo, and J. Hulin, Phys. Fluids A **2**, 681 (1990).